The Astrophysical Journal, 850:85 (7pp), 2017 November 20 https://doi.org/10.3847/1538-4357/aa932f

The Putative Cerean Exosphere

Norbert Schorghofer[1], Shane Byrne[2], Margaret E. Landis[2], Erwan Mazarico[3], Thomas H. Prettyman[1], Britney E. Schmidt[4], Michaela N. Villarreal[5], Julie Castillo-Rogez[6], Carol A. Raymond[6], and Christopher T. Russell[5]
[1] Planetary Science Institute, Tucson, AZ 85719, USA
[2] University of Arizona, Tucson, AZ 85721, USA
[3] NASA Goddard Spaceflight Center, Greenbelt, MD 20771, USA
[4] Georgia Institute of Technology, Atlanta, GA 30332, USA
[5] University of California, Los Angeles, CA 90095, USA
[6] Jet Propulsion Laboratory, Pasadena, CA 91109, USA
Received 2017 August 4; revised 2017 October 5; accepted 2017 October 10; published 2017 November 20

Abstract

The ice-rich crust of dwarf planet 1 Ceres is the source of a tenuous water exosphere, and the behavior of this putative exosphere is investigated with model calculations. Outgassing water molecules seasonally condense around the winter pole in an optically thin layer. This seasonal cap reaches an estimated mass of at least 2×10^3 kg, and the aphelion summer pole may even retain water throughout summer. If this reservoir is suddenly released by a solar energetic particle event, it would form a denser transient water exosphere. Our model calculations also explore species other than H_2O. Light exospheric species escape rapidly from Ceres due to its low gravity, and hence their exospheres dissipate soon after their respective source has faded. For example, the theoretical turn-over time in a water exosphere is only 7 hr. A significant fraction of CO_2 and SO_2 molecules can get trapped and stored in perennially shadowed regions at the current spin axis orientation, but not at the higher spin axis tilt, leaving H_2O as the only common volatile expected to accumulate in polar cold traps over long timescales. The D/H fractionation during migration to the cold traps is only about 10%.

Key words: minor planets, asteroids: individual (Ceres) – molecular processes – solid state: volatile

1. Introduction

Exospheric species have been detected on large airless bodies, especially on Earth's Moon and the planet Mercury (Killen & Ip 1999; Stern 1999). Ceres, the largest body in the main asteroid belt, has abundant subsurface ice at a shallow depth (Prettyman et al. 2017), and therefore it must have a tenuous water exosphere. Detection of an atmosphere on Ceres has been reported, but the occurrence is only episodic (A'Hearn & Feldman 1992; Rousselot et al. 2011; Küppers et al. 2014; Roth et al. 2016). No instrument on the Dawn spacecraft was designed to detect an exosphere, but observations during the initial highest-altitude orbit yielded no evidence of forward-scattered light that a dust-carrying atmosphere would have produced (Russell et al. 2016). Evidence of haze on Ceres (Nathues et al. 2015; Thangjam et al. 2016) is controversial (Schröder et al. 2017). However, the detection of energetic electrons on three successive spacecraft orbits after a solar proton event can be interpreted as the by-product of a transient atmosphere (Russell et al. 2016; Jia et al. 2017; Villarreal et al. 2017).

Here, we study the properties of exospheres on Ceres, based on a numerical model of molecules that travel on ballistic trajectories at thermal speeds. The dynamics of exospheres with an exobase has long been studied (e.g., Öpik and Singer 1959), but here a surface-bounded exosphere is considered. Tu et al. (2014) and Schorghofer et al. (2016) previously modeled the cerean water exosphere. The behavior of a denser water atmosphere on Ceres was modeled by Küppers et al. (2014) and Formisano et al. (2016). The present modeling work is restricted to collisionless thermalized exospheres of neutral atoms and molecules. An exosphere redistributes volatile molecules over the entire surface of the dwarf planet, including the polar regions. Fanale & Salvail (1989) and Hayne & Aharonson (2015) considered the possibility of a permanent polar cap and concluded it would require an implausibly high albedo.

We also put the putative exosphere of Ceres in context with those on Earth's Moon and Mercury. All three bodies have permanently shadowed craters near their rotational poles, where ices can accumulate (Arnold 1979). The axis tilt of Ceres oscillates between 2° and 20° with a period of 24.5 kyr (Bills & Scott 2017; Ermakov et al. 2017), so it becomes necessary to distinguish between permanent and perennial shadows. Several of the perennially shadowed regions (PSRs) on Ceres contain bright deposits (Platz et al. 2017; Ermakov et al. 2017).

2. Potential Exospheric Species

Ceres has a crust rich in water ice (Prettyman et al. 2017), and over time these molecules diffuse through the overlying porous layer, emerge on the surface, and continuously supply a water exosphere. Other chemical species could be occasionally delivered to the main belt (e.g., CO_2 ice from comet impacts) or percolate up from the interior (e.g., Ar-40 from decay of K-40). Here we explore a number of candidate species by quantifying their exospheric lifetimes.

A molecule in contact with the surface quickly thermalizes and a mole acquires a kinetic energy of $(3/2)RT$, where R is the universal gas constant and T is the surface temperature. The Maxwell distribution for the launch velocity v is

$$P_M(v) = \frac{4s^{3/2}}{\sqrt{\pi}} v^2 e^{-sv^2} \qquad s = \frac{\mu}{2RT}, \tag{1}$$

where μ is molar mass.

On the Moon, the daytime altitude distribution of argon is better explained with an Armand velocity distribution than with

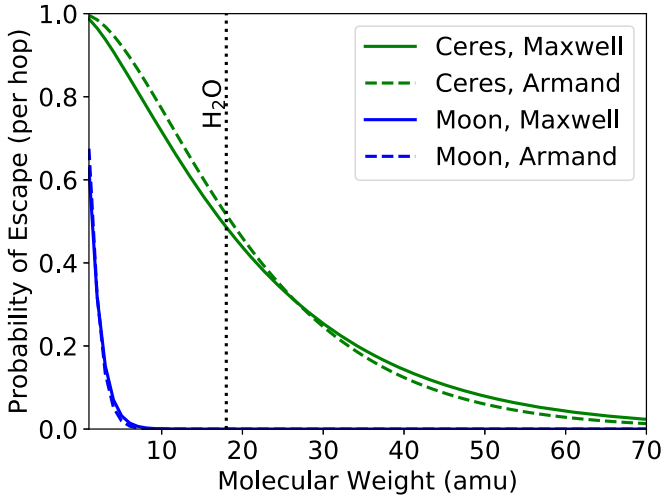

Figure 1. Probability of gravitational escape per hop for Ceres ($T = 237$ K, $v_e = 517$ m s^{-1}) and Earth's Moon ($T = 387$ K, $v_e = 2372$ m s^{-1}).

a Maxwell distribution (Hodges & Mahaffy 2016). An Armand distribution is indeed expected for a desorption process. This probability distribution is

$$P_A(v) = 2s_A^2 v^3 e^{-s_A v^2} dv \qquad s_A = \frac{2\mu}{3RT}. \tag{2}$$

The expression has the required properties

$$\int_0^\infty P_A(v)\, dv = 1, \tag{3}$$

$$\frac{\mu}{2}\int_0^\infty v^2 P_A(v)\, dv = \frac{3}{2}RT. \tag{4}$$

The same two properties hold for P_M, Equation (1), of course.

The fraction of molecules that escapes gravitationally, in the tail of the thermal velocity distribution, can be estimated analytically. For a Maxwell distribution (1), the probability that a molecule is above the escape velocity v_e is

$$\beta_M = \int_{v_e}^\infty P_M(v)dv = 1 - \mathrm{Erf}(v_e\sqrt{s}) + 2v_e\sqrt{\frac{s}{\pi}}e^{-sv_e^2}. \tag{5}$$

For the Armand distribution (2), this fraction is

$$\beta_A = \int_{v_e}^\infty P_A(v)dv = (1 + s_A v_e^2)e^{-s_A v_e^2}. \tag{6}$$

Figure 1 shows the escape probability β for the Maxwell and the Armand distributions as a function of molecular weight. A single temperature (the subsolar temperature) is assumed for simplicity. Both velocity distributions lead to similar escape rates. In contrast to the Moon, gravitational escape is significant on Ceres even for heavy species.

Table 1 lists a number of candidate species. For gravitational (Jeans) escape rates, the probabilities (5) and (6) are expressed per hop instead of per time. The light species are all dominated by gravitational escape and are short lived. For example, H_2O typically undergoes only two hops, although it may reside on the nighttime surface during this migration. Escape rates per time for non-uniform gravity are difficult to calculate analytically, and the exospheric half-life of H_2O will be provided below as the result of a comprehensive numerical model. One hop of a H_2O molecule takes a few hours on average, and less for heavier species.

Table 1
Gravitational (Jeans) Escape Probabilities β_M and Timescales for Photo-destruction τ_{photo} on Ceres for a List of Candidate Species

Species	μ (amu)	β_M (per hop)	τ_{photo}
He-4	4.003	0.89	5 years
NH_3	17.03	0.43	12 hr
H_2O	18.01	0.41	7 days
HDO	19.02	0.38	7 days
Ar-40	40	0.092	9 months
CO_2	44.01	0.070	44 days
SO_2	64.06	0.016	10 hr
Xe	131.3	1.0×10^{-4}	59 days

Note. The gravitational escape rate is calculated for 200 K, representative of the daytime temperatures. The photo-destruction time is for continuous exposure (dayside) at normal sun activity.

Photo-destruction rates are based on the compilation by Huebner et al. (1992) and scaled by $1/a^2$, where a is the semimajor axis of the orbit around the Sun. The photo-destruction timescale τ_{photo} in Table 1 only applies to the time the molecule or atom spends exposed to sunlight. The residence time in the exosphere is limited by gravitational escape and photo-destruction, but the former dominates for most species. Among the species listed, photo-destruction loss is significant only for SO_2 and Xe, and xenon is the longest-lived. It lasts longer than it would on the Moon, where photo-destruction proceeds faster.

The crossover from a collisionless exosphere to a true atmosphere corresponds to a specific density. In a uniform gas, the mean-free path is given by $\ell = 1/\sqrt{2}n\pi\sigma^2$, where n is the volumetric number density and $\pi\sigma^2$ is the collisional cross section. For neutral H_2O, $\sigma = 2.7$ Å (Schwertz & Brow 1951). For uniform gravity, the scale height is $H = RT/\mu g$. From simple mechanics it follows that the maximum height of a ballistic trajectory is $v_z^2/(2g)$, and combined with the equipartition theorem, the average maximum height of thermal ballistic hops is $H/2$, or about 160 km. If the mean-free path equals the scale height, then the density below which the assumption of a collisionless exosphere is justified is $n \approx 2 \times 10^{13}$ molec m^{-3}. This is above the densities modeled by Küppers et al. (2014) to match their observations. The mass of such a transition exosphere/atmosphere is on the order of 4×10^5 kg. If condensed and uniformly distributed over the surface, it would be barely a monolayer thick.

3. Monte-Carlo Model and Seasonal Condensation of H_2O

3.1. Model Description

The ballistic trajectories of atoms and molecules are simulated with a Monte-Carlo method. Individual molecules are launched with probabilistically distributed cartesian velocity components that amount to a random initial azimuth, launch angle, and thermal speed appropriate for the local surface temperature. The model then computes the molecule's impact location and time analytically, taking into account the radial dependence of the gravitational acceleration. An event-driven algorithm is used, where landing and launching events are processed in time-order. The detailed equations and further description are included in the user guide that accompanies the source code archived at https://github.com/nschorgh/Planetary-Code-

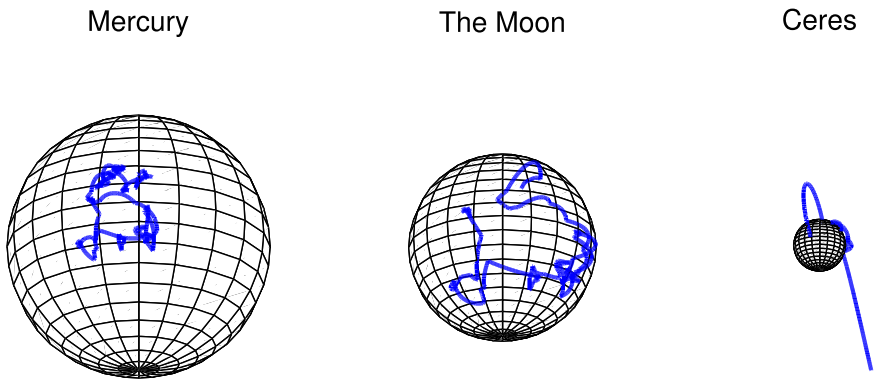

Figure 2. Comparison of ballistic hops of water molecules on Mercury, the Moon, and Ceres based on model calculations.

Collection/ and 10.5281/zenodo.1001854 (Schörghofer 2017), but an outline of the ballistic trajectory calculations is provided in the following.

For constant gravitational acceleration g, the flight distance d and flight duration t are

$$d = \frac{2}{g} v_3 \sqrt{v_1^2 + v_2^2}, \tag{7}$$

$$t = 2v_3/g, \tag{8}$$

where (v_1, v_2, v_3) are the initial velocity components along longitude, meridian, and vertical direction, respectively. For radially dependent gravitational acceleration, d and t can also be calculated analytically. Instead of (7) and (8),

$$\alpha = \arctan\left(\sqrt{v_1^2 + v_2^2}\big/ v_3\right), \tag{9}$$

$$\gamma = (|\vec{v}|/v_e)^2, \tag{10}$$

$$e = \sqrt{1 - 4\gamma(1-\gamma)\sin^2\alpha}, \tag{11}$$

$$d = 2R_b \arccos\left(\frac{1 - 2\gamma\sin^2\alpha}{e}\right), \tag{12}$$

$$E_p = \pi - 2\arctan\left(\sqrt{\frac{1-e}{1+e}}\Big/ \tan\frac{d}{4R_b}\right), \tag{13}$$

$$t = \frac{R_b}{v_e}\frac{E_p + e\sin E_p}{(1-\gamma)^{3/2}}, \tag{14}$$

where α is the zenith angle of the launch velocity, e is the eccentricity of the ballistic trajectory, and R_b is the radius of the body. These equations are derived from those in Vogel (1966) and Kegerreis (2015).

A ballistic trajectory lies on a plane that goes through the center of the body, and the ground track is thus part of a great circle. With starting coordinates (λ_1, ϕ_1), the landing coordinates $(\lambda_2, \phi_1 + \Delta\phi)$ are given by

$$\cos a_z = v_2\big/\sqrt{v_1^2 + v_2^2}, \tag{15}$$

$$\sin\lambda_2 = \sin\left(\frac{d}{R_b}\right)\cos\lambda_1\cos a_z + \sin\lambda_1\cos\left(\frac{d}{R_b}\right), \tag{16}$$

$$\cos\Delta\phi = \frac{\cos\left(\frac{d}{R_b}\right)\cos\lambda_1 - \sin\lambda_1\sin\left(\frac{d}{R_b}\right)\cos a_z}{\cos\lambda_2}, \tag{17}$$

where a_z is the launch azimuth. The Coriolis effect is incorporated by adding to the longitudinal component of the launch velocity and subtracting the rotation over the duration of flight.

Figure 2 illustrates thermal ballistic hops obtained with this model for artificial uniform surface temperature. Since the model calculates the landing position analytically without integrating the trajectory, an extraneous numerical integrator was used to create this illustration. This comparison also allowed for cross-validation of the results. On Mercury and the Moon, the water molecule is eventually destroyed by photodissociation. On Ceres, it escapes to space (Figure 2).

The full model of the exosphere also requires surface temperatures that vary geographically and with time and a quantification of molecular residence times. Surface temperatures are calculated on a geographic grid of one-dimensional thermal models, and agree with the results of Hayne & Aharonson (2015). The shape of Ceres is approximated with a sphere of 470 km radius (volumetric mean).

On the Moon and on Mercury, the molecular surface residence time is negligible compared to the flight time on most of the dayside and the reverse is the case on most of the night side. On Ceres, this distinction is less valid. Due to the colder temperatures, surface residence times can be long even in sunlit areas near the poles. Residence times are based on vapor pressure relations (Schorghofer & Taylor 2007). For example, at 200 K the model residence time is 2 ms, and at 110 K it is almost one cerean year.

A Sun elevation of 3° corresponds to an equilibrium temperature of 110 K. In other words, seasonal condensation can be expected in sunlit regions, up to 3° latitude beyond polar winter. With an obliquity of 4°, a seasonal cap can be expected to extend to latitudes of roughly 83°. Adsorbed water molecules have longer residence times than those of ice, so seasonal condensation can be expected over an even larger area.

In the model, molecular residence times themselves are distributed probabilistically. An exponential distribution for $1/t$ is proportional to $e^{-\tau/t}d(1/t)$. The normalized probability distribution for t is then

$$P(t) = \frac{\tau}{t^2}e^{-\tau/t}, \tag{18}$$

which obeys the desired relations

$$\int_0^\infty P(t)\,dt = 1, \tag{19}$$

$$\int_0^\infty \frac{1}{t} P(t)\, dt = \frac{1}{\tau}. \quad (20)$$

Destruction by space weathering and solar wind takes place while a molecule resides on the surface. According to Lanzerotti et al. (1981), the highest of these erosion rates is 10^{12} molec m^{-2} s^{-1} for an ice layer. Since a monolayer of water corresponds to about 10^{19} molec m^{-2}, these loss rates are lower than in-flight photo-destruction.

3.2. Model Results

Figure 3(a) shows a snapshot of water molecules on the globe, which reveals a build-up of molecules residing in the polar region. Hence there is seasonal condensation in the polar regions, the equivalent of a seasonal polar cap, but the amount of water involved is so small that it does not change the albedo of the surface. The assumed source locations of the molecules lie within 40° of the equator, where most of the ice retreat takes place. Latitude × longitude resolution was (1/2)° × 15°.

Figure 3(b) shows the number of computational water molecules on the surface and in-flight as a function of time. The number of in-flight (and gravitationally bound) molecules barely varies with the season. The same model calculation involved a supply of ten molecules every 10 minute time step. On average about 410 molecules are in-flight at any time, which corresponds to the supply over 7 hr. This represents the half-life of the exosphere. It is shorter than that modeled by Formisano et al. (2016) for a denser atmosphere. The variations detected by the Herschel telescope over the 9 hr rotation period have been interpreted as regional variation (Küppers et al. 2014); instead they may be consistent with a decaying density.

Figure 3(b) also shows the number of computational water molecules that reside on the surface, which reveals two maxima per orbit, as expected for a seasonal phenomenon. Up to nearly 10^4 computational molecules reside on the surface, the equivalent of about one week of supply. If outgassing rates are 0.003 kg s^{-1} (Prettyman et al. 2017), this amounts to up to $\sim 2 \times 10^3$ kg of water on the surface. Spread from the winter pole to a latitude of 83° ($\sim 10^{10}$ m^2), its thickness is a monolayer.

However, this is the lowest plausible mass estimate. First, the residence time of H_2O on silicate surfaces is longer than that for H_2O on ice. Based on adsorption isotherm measurements on lunar samples by Cadenhead & Stetter (1974), the residence times can be parametrized as a function of surface density (Schorghofer & Aharonson 2014). With this extrapolation, molecules in a single monolayer have five times longer residence times, and for 1/10 of a monolayer residence times are 400 times longer than for that of a thick ice layer. This leads to a larger seasonal "cap." Second, the aphelion summer pole may be cold enough to retain ice, leading to a build-up from orbit to orbit. Figure 3(b) represents a circular orbit, and results for the current eccentric orbit are shown in Figure 3(c), which reveals an increase in cap mass from orbit to orbit, because the north polar region retains ice even through the summer solstice. Third, the outgassing rate of 0.003 kg s^{-1} is by itself a low estimate, and could be considerably higher. This model estimate depends on grain size and thermal inertia, and both are only crudely constrained by existing observations. Pre-dawn mission model estimates put the outgassing rate two orders of magnitude higher (Fanale & Salvail 1989; Schorghofer 2016). The outgassing may also vary seasonally. In summary, the mass of the seasonal cap is difficult to estimate, but 2×10^3 kg with monolayer thickness is a minimum estimate. It could well be an order of magnitude more massive, but still optically thin.

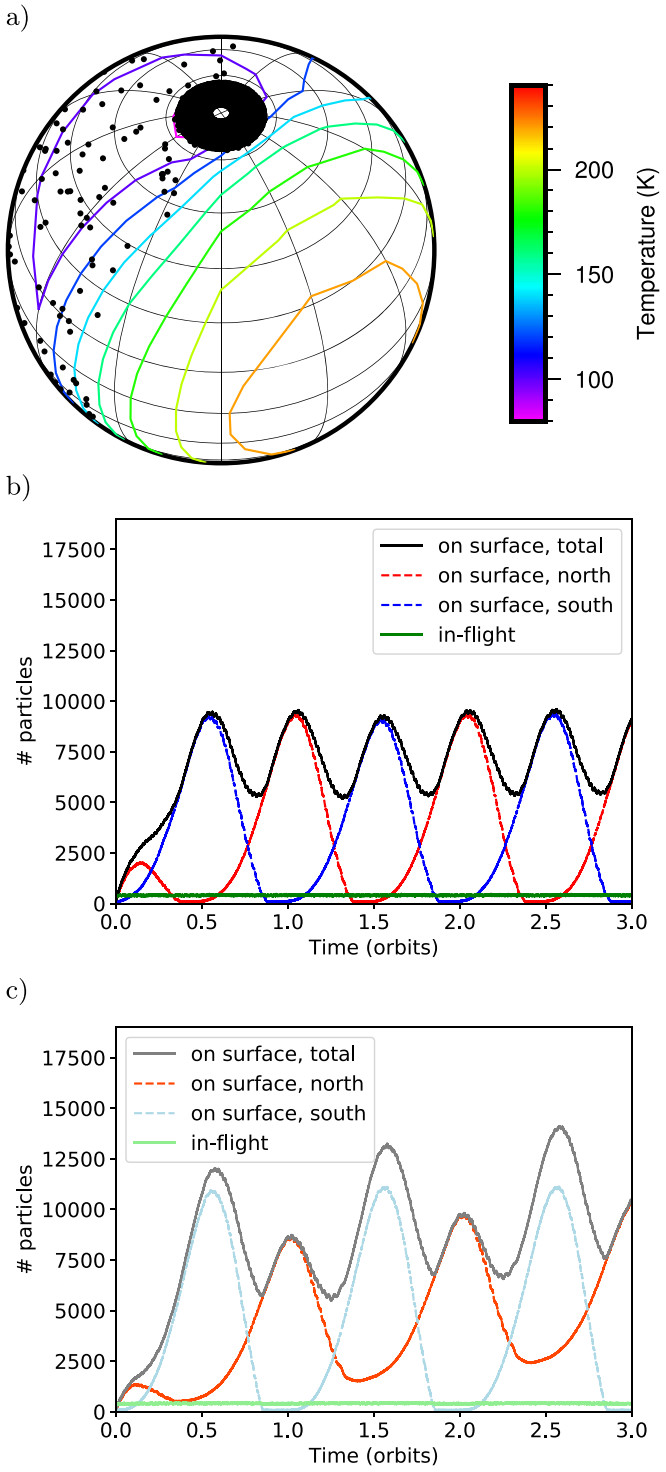

Figure 3. (a) Snapshot of water molecules (black dots) temporarily residing on the surface of Ceres according to model calculations. Note the molecules around the winter pole. The tiny white area at the pole is the cold trap, and the many cold-trapped molecules are not shown. The contours are the surface temperature. (b) Number of water molecules residing on the surface and in-flight as a function of time for circular orbit. The supply rate is one computational particle per minute, and the vertical axis can also be interpreted as the supply-equivalent in units of minutes. For example, 10,000 computational particles correspond to about one week of supply. (c) Number of water molecules residing on the surface and in-flight as a function of time for eccentric orbit.

The lack of optically bright deposits in PSRs illuminated during the most recent obliquity maximum, about 14 kyr ago (Ermakov et al. 2017), places an upper bound on the delivery of water to the polar regions over this time period. If we assume a 100 μm thick layer would be optically thick, this corresponds to a delivery of <7 nm yr^{-1}. A monolayer is about 0.3 nm thick. For the supply of half an orbit, this upper bound is only 50 times the minimum mass estimate for the seasonal cap above, or 10^5 kg.

3.3. Discussion

Whereas the existence of a tenuous water exosphere is fully expected, no satisfactory explanation for an episodic atmosphere has emerged yet. It could be caused by mass wasting events or impacts, but such events are rare. Ice patches exposed on the sunlit surface (Combe et al. 2016) are few and small, and produce little vapor (Landis et al. 2017). Ice deposits in perennially shadowed craters are also small and few in number (Ermakov et al. 2017; Platz et al. 2017), and moreover the Herschel observations suggest that the vapor did not originate from the polar regions (Küppers 2017). The episodic appearance of a cerean exosphere is correlated with solar energetic particle (SEP) events (Villarreal et al. 2017), but the specific source of water remains an open question. Near-surface ice would be rapidly depleted, even if it was possible for an SEP event to release it at a sufficient rate.

To add to the list of candidate mechanisms, we propose a seasonal cap released by an SEP event as a possible source for an episodic exosphere or atmosphere. This "cap" resides on the surface where it can be easily eroded, and renews itself twice a cerean year. A potentially observable consequence is the depletion of the reservoir. If a sufficiently large SEP event depletes the entire cap, a second SEP event that follows a short time later would not release a significant amount of water. It takes on the order of half a cerean year to fully rebuild the seasonal cap. There is also a dependence of the cap mass on the season, but because the seasonal cap extends into sunlit regions, part of it even exists during equinoxes and the total mass varies by less than a factor of two over one orbit (Figures 3(b), (c)).

Küppers et al. (2014) used a steady-state atmosphere to model their observations rather than an episodic exosphere, so a detailed comparison is not possible. But an exosphere of 2×10^3 kg distributed over 160 km height corresponds to a density of $n = 1 \times 10^{11}$ molec m^{-3}, which is typical for the densities shown in Extended Data Figure 2 of Küppers et al. (2014). Hence, the seasonal cap may be massive enough to explain these observational measurements.

However, an SEP-mobilized seasonal cap as source of a transient atmosphere is not without inconsistencies either. The timing and frequency of events may be incompatible with past observational constraints. An SEP-generated exosphere should decay on a timescale of 7 hr, and a cap needs many months to rebuild. Such episodic outbursts would be too infrequent to be compatible with all of the existing observations.

In a steady-state, an exosphere with the aforementioned mass and density can be sustained with a water source rate of 0.08 kg s^{-1} (2×10^3 kg every 7 hr). Compared to the end-member model where molecules stream out radially with a thermal velocity of 800 m s^{-1}, a near-surface density of 10^{11} molec m^{-3} would require 30 kg s^{-1}. This difference of more than two orders of magnitude is due to the fact that the water exosphere is gravitationally bound, and therefore concentrated in a much smaller volume and populated with recycled molecules.

Table 2
Fraction of Molecules Trapped

Species	Obliq. ϵ (°)	Source	Trap Area (%)	Fraction Trapped (%)	Trapping Efficiency
H_2O	4	equat.	0.13	0.16	1.2
H_2O	4	uniform	0.13	0.21	1.6
H_2O	4	uniform	0.15	0.24	1.6
H_2O	2	uniform	0.24	0.38	1.6
H_2O	10	uniform	0.013	0.02	1.6
HDO	4	uniform	0.13	0.23	1.8
HDO	2	uniform	0.24	0.41	1.7

Note. The trapping efficiency is the ratio of the relative trapping area to the fraction of molecules trapped.

4. Cold-trapping of Ices

Condensible species, such as water ice, ammonia, carbon dioxide, and sulfur dioxide, can accumulate in cold traps (Zhang & Paige 2009), and the exosphere can transport these molecules from any location on the surface of the dwarf planet into the cold traps. Model calculations are carried out to determine the fraction of molecules that are trapped instead of lost. They involve a steady-state exosphere, where sources and sinks balance statistically. Cold traps are represented by a circular area around the rotational poles with equal area at both poles. Unless stated otherwise, the source of water molecules is assumed to be geographically uniform (same number of molecules per area), but cold traps are excluded as source locations. First we turn to cold-trapping from the water exosphere.

Due to the seasonal condensation phenomenon, model calculations for the trapping in the PSRs must proceed over several orbits rather than only several solar days. Table 2 shows the model results for various scenarios. The first row corresponds to an equatorial source of water molecules, within $\pm 40°$, as was assumed in Section 3 and in Schorghofer et al. (2016). The second row corresponds to a geographically uniform source, where a slightly higher fraction is captured, because launch velocities are lower at the more polar latitudes and the source is on average closer to the cold traps. The third row uses a cold trap area in line with the area estimate from the stacking of Framing Camera images (Platz et al. 2017), instead of the illumination modeling (Schorghofer et al. 2016). The fourth row involves simulations at minimum obliquity, 2°, and the correspondingly larger cold trap area, and the fifth row is for an obliquity of 10°, and the correspondingly smaller cold trap area (Ermakov et al. 2017). The trapping efficiency, which is proportional to the rate at which the thickness of the ice deposits grows, is the same in all four cases. In other words, for H_2O on Ceres the fraction trapped is proportional to the cold trap area, even if the obliquity changes. Species that undergo many hops do not have a constant trapping efficiency.

The last two rows in Table 2 are for HDO molecules. Since D/H is a tracer for the source of water, a question that will one day be relevant is to what extent the D/H of cold-trapped ice is representative of the D/H of the source, i.e., the isotopic fractionation that occurs during the migration to the cold traps.

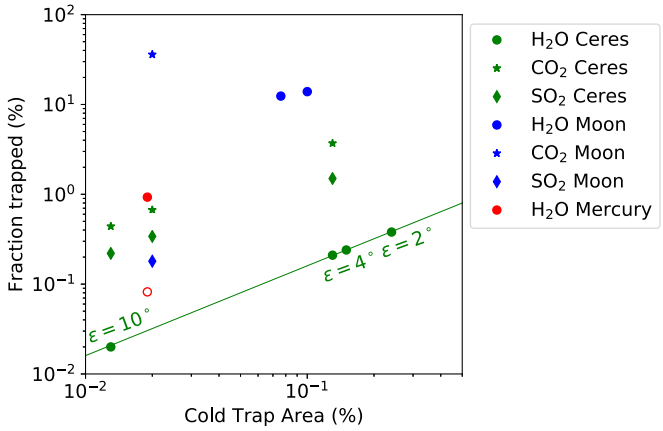

Figure 4. Trapping fraction for several molecular species as a function of the cold trap area.

For example, on the Moon this fractionation is expected to be small (Crider & Vondrak 2000; Schorghofer 2014). For the present-day obliquity and cold trap area of Ceres $[HDO]/[H_2O] = 1.12 \pm 0.01$, where the error estimate is purely statistical due to the finite number of computational particles. For a 2° obliquity and the correspondingly larger trapping area $[HDO]/[H_2O] = 1.10 \pm 0.02$. This fractionation is significantly smaller than the difference in the D/H ratio of known reservoirs (e.g., solar wind, standard mean ocean water, or comets).

Figure 4 compares the trapping fractions for H_2O on Ceres with those on the Moon and on Mercury; the axes are logarithmic. All results were obtained with the same model implementation. The Moon traps two orders of magnitude more of the available molecules than Ceres. Two source scenarios are shown for Mercury: one where the source is uniformly distributed (solid red circle) and one where the source is restricted to surface temperatures above 400 K (empty red circle). The trapping fraction is lower in the latter case, because these molecules start farther from the polar regions, and on Mercury loss is due to photo-destruction, such that longer travel times lead to more loss.

Figure 4 also includes CO_2 and SO_2, although their respective cold-trapping areas have not yet been determined. These substances are more volatile than H_2O, so their respective trap areas are smaller than that for H_2O, but larger than zero (Schorghofer et al. 2016). In areas that are cold enough, both types of molecules are trapped efficiently. Trapping efficiencies were not calculated for NH_3, because ammonia has a higher photo-destruction cross section than H_2O and is lighter than H_2O (Table 1), so its trapping efficiency must be smaller than that for H_2O. For argon and xenon, PSRs are not cold enough to expect trapping.

In bowl-shaped craters, shaped as the cap of a sphere, the indirect scattering of visible and infrared radiation can be evaluated with a simple theoretical formula (Buhl et al. 1968; Ingersoll et al. 1992). Schorghofer et al. (2016) have illustrated these temperatures for Ceres. At current obliquity, 4°, CO_2, SO_2, and NH_3 could be trapped in shallow PSRs near the rotational poles. At a maximum obliquity of 20°, this is no longer the case. Bright deposits are observed in the few areas that remain shadowed even at maximum obliquity (Ermakov et al. 2017), which is consistent with cold-trapped water ice.

5. Conclusions

The water exosphere of Ceres seasonally condenses around the winter pole, creating an optically thin polar cap. Using conservative assumptions for the source rate and molecular surface residence times, the estimated mass of this seasonal cap is on the order of 2×10^3 kg. A higher mass is plausible, but 10^5 kg is an estimated upper limit based on the lack of optically thick ice in recent PSRs. An SEP event could transform this seasonal reservoir into a short-lived transient exosphere with a mass consistent with those of existing observations.

The fraction of the water exosphere that is captured in PSRs experiences a small isotopic fractionation from the source to the cold traps, $[HDO]/[H_2O] \approx 1.1$. CO_2 molecules are trapped very efficiently. The trapping efficiency of SO_2 lies in between that of CO_2 and H_2O. The fraction of NH_3 captured is less than that of H_2O. A significant fraction of CO_2 and SO_2 molecules can get trapped and stored in PSRs at the current spin axis orientation, but not at a higher spin axis tilt, leaving H_2O as the only common volatile that can accumulate over long timescales.

Gravitational escape rates are large, so exospheres dissipate soon after their respective source disappears. The half-life of a water exosphere is 7 hr. Only for some heavy species, SO_2 and Xe, is loss by photo-destruction comparable to that of gravitational escape.

We thank Vincent Eke, Lucy McFadden, Stefano Mottola, an anonymous reviewer, and the Dawn science team for insightful discussions. N.S. was supported by the National Aeronautics and Space Administration under Grant No. NNX15AI38G and 80NSSC17K0545 issued through the Dawn at Ceres Guest Investigator Program (DACGIP).

ORCID iDs

Norbert Schorghofer https://orcid.org/0000-0002-5821-4066
Shane Byrne https://orcid.org/0000-0002-6735-4685
Margaret E. Landis https://orcid.org/0000-0001-7321-2272
Erwan Mazarico https://orcid.org/0000-0003-3456-427X
Thomas H. Prettyman https://orcid.org/0000-0003-0072-2831
Britney E. Schmidt https://orcid.org/0000-0001-7376-8510
Michaela N. Villarreal https://orcid.org/0000-0003-1947-7741
Julie Castillo-Rogez https://orcid.org/0000-0003-0400-1038
Carol A. Raymond https://orcid.org/0000-0002-4213-8097
Christopher T. Russell https://orcid.org/0000-0003-1639-8298

References

A'Hearn, M. F., & Feldman, P. D. 1992, Icar, 98, 54
Arnold, J. R. 1979, JGR, 84, 5659
Bills, B. G., & Scott, B. R. 2017, Icar, 284, 59
Buhl, D., Welch, W. J., & Rea, D. G. 1968, JGR, 73, 5281
Cadenhead, D. A., & Stetter, J. R. 1974, in Proc. 5th Lunar Conf., 2301
Combe, J.-P., McCord, T. B., Tosi, F., et al. 2016, Sci, 353, aaf3010
Crider, D. H., & Vondrak, R. R. 2000, JGR, 105, 26773
Ermakov, A. I., Mazarico, E., Schröder, S. E., et al. 2017, GeoRL, 44, 2652
Fanale, F. P., & Salvail, J. R. 1989, Icar, 82, 97
Formisano, M., De Sanctis, M., Magni, G., Federico, C., & Capria, M. 2016, MNRAS, 455, 1892
Hayne, P. O., & Aharonson, O. 2015, JGR, 120, 1567
Hodges, R. R., & Mahaffy, P. R. 2016, GeoRL, 43, 22
Huebner, W. F., Keady, J. J., & Lyon, S. P. 1992, A&SS, 195, 1
Ingersoll, A. P., Svitek, T., & Murray, B. C. 1992, Icar, 100, 40
Jia, Y.-D., Villarreal, M. N., & Russell, C. T. 2017, JGR, 122, 4976
Kegerreis, J. 2015, Master's Thesis, Durham Univ.
Killen, R. M., & Ip, W.-H. 1999, RvGeo, 37, 361

Küppers, M. 2017, European Planetary Science Congress 11, Abstract, 197 (http://meetingorganizer.copernicus.org/EPSC2017/EPSC2017-197.pdf)
Küppers, M., O'Rourke, L., Bockelée-Morvan, D., et al. 2014, Natur, 505, 525
Landis, M. E., Byrne, S., Schorghofer, N., et al. 2017, JGR, in press, https://doi.org/10.1002/2017JE005335
Lanzerotti, L. J., Brown, W. L., & Johnson, R. E. 1981, JGR, 86, 3949
Nathues, A., Hoffmann, M., Schaefer, M., et al. 2015, Natur, 528, 237
Öpik, E. J., & Singer, S. F. 1959, PhFl, 2, 653
Platz, T., Nathues, A., Schorghofer, N., et al. 2017, NatAs, 1, 7
Prettyman, T. H., Yamashita, N., Toplis, M. J., et al. 2017, Sci, 355, 55
Roth, L., Ivchenko, N., Retherford, K. D., et al. 2016, GeoRL, 43, 2465
Rousselot, P., Jehin, E., Manfroid, J., et al. 2011, AJ, 142, 125
Russell, C. T., Raymond, C. A., Ammannito, E., et al. 2016, Sci, 353, 1008
Schorghofer, N. 2014, GeoRL, 41, 4888
Schorghofer, N. 2016, Icar, 276, 88
Schörghofer, N. 2017, Planetary-Code-Collection: Thermal and Ice Evolution Models for Planetary Surfaces v1.1.4, Zenodo, 10.5281/zenodo
Schorghofer, N., & Aharonson, O. 2014, ApJ, 788, 169
Schorghofer, N., Mazarico, E., Platz, T., et al. 2016, GeoRL, 43, 6783
Schorghofer, N., & Taylor, G. J. 2007, JGR, 112, E02010
Schröder, S., Mottola, S., Carsenty, U., et al. 2017, Icar, 288, 201
Schwertz, F. A., & Brow, J. E. 1951, JChPh, 19, 640
Stern, S. A. 1999, RvGeo, 37, 453
Thangjam, G., Hoffmann, M., Nathues, A., Li, J.-Y., & Platz, T. 2016, ApJL, 833, L25
Tu, L., Ip, W.-H., & Wang, Y.-C. 2014, P&SS, 104, 157
Villarreal, M. N., Russell, C. T., Luhmann, J. G., et al. 2017, ApJL, 838, L8
Vogel, U. 1966, P&SS, 14, 1233
Zhang, J. A., & Paige, D. A. 2009, GeoRL, 36, L16203